Journal of
Synchrotron
Radiation

ISSN 0909-0495

Received 21 September 2010
Accepted 12 December 2010

A large-volume gas cell for high-energy X-ray reflectivity investigations of interfaces under pressure

Federica Venturini,[a,b]* Sebastian Schöder,[b] Werner F. Kuhs,[c] Veijo Honkimäki,[b] Louis Melesi,[d] Harald Reichert,[b] Helmut Schober[d] and Frederic Thomas[d]

[a]Diamond Light Source Ltd, Diamond House, Harwell Science and Innovation Campus, Didcot, Oxfordshire OX11 0DE, UK, [b]European Synchrotron Radiation Facility, BP 220, 38043 Grenoble, France, [c]Universität Göttingen, GZG, Goldschmidtstrasse 1, 37077 Göttingen, Germany, and [d]Institut Laue Langevin, BP 156, 38042 Grenoble, France.
E-mail: federica.venturini@diamond.ac.uk

A cell for the investigation of interfaces under pressure is presented. Given the pressure and temperature specifications of the cell, $P \leq 100$ bar and 253 K $\leq T \leq$ 323 K, respectively, high-energy X-rays are required to penetrate the thick Al_2O_3 windows. The CH_4 (gas)/H_2O (liquid) interface has been chosen to test the performance of the new device. The measured dynamic range of the high-energy X-ray reflectivity data exceeds 10^{-8}, thereby demonstrating the validity of the entire experimental set-up.

Keywords: interfaces under pressure; high-energy X-ray reflectivity; gas hydrates.

1. Introduction

Interfaces unavoidably exist in any real system. Any time a two-dimensional interface is encountered, specific phenomena are likely to happen. Both in nature and in technology, more often than not, the most interesting interfacial phenomena occur at the interface between bulk systems. Well known examples of 'buried' interfaces in our every day life are: two immiscible liquids in contact with each other, like water and oil; cellular membranes operating under the physiological conditions present in our body; artificially bonded wafers, nowadays commonly used in microelectronics. Because of the strong X-ray attenuation coefficient, buried interfaces such as these are difficult to access with conventional X-rays ($E \simeq$ 10 keV) and it is only the relatively recent advent of high-brilliance high-energy X-ray sources that has allowed scientists to start addressing these more realistic and complex interfacial phenomena (Roser *et al.*, 1994; Huisman *et al.*, 1997; Reichert *et al.*, 2000, 2003; Richter *et al.*, 2000; Rieutord *et al.*, 2001; Engemann *et al.*, 2004; Tikhonov *et al.*, 2004; Schlossman, 2005; Baigl *et al.*, 2005; Miller *et al.*, 2005; Mezger *et al.*, 2008*a*,*b*; Lehmkühler *et al.*, 2009; Schöder *et al.*, 2009).

Pressure plays an important role in many interfacial interactions. The pressure-induced adsorption of molecules on liquid surfaces is, for example, a focus of current interest (Ragil *et al.*, 1996; Bertrand *et al.*, 2000; Paulus *et al.*, 2005, 2008). Since pressure is a key variable in geological systems, a whole variety of phenomena, that range from mineral-fluid interactions in the crust of our planet (Dysthe *et al.*, 2006) to the migration of gases within the barriers engineered for safe underground nuclear waste disposal (Galle, 2000), are heavily influenced by this parameter. Heterogeneously and homogeneously catalyzed reactions also take place at high pressures (Grunwaldt & Baiker, 2005; Grunwaldt *et al.*, 2005). In this context, given their unusual physical and transport properties, supercritical fluids have recently proven to be advantageous media for such processes. In biophysics various physiological properties of cell membranes, such as permeability and synaptic transmission amongst others, are known to be influenced by pressure (MacDonald, 1984).

Here we present a novel chamber that has been specifically designed for the investigation of pressurized interfaces by means of high-energy X-ray reflectivity, a technique that probes the variation of the electron density, $\rho_e(z)$, in the direction that is perpendicular to the interface, with angstrom resolution. To the best of our knowledge the device described in the following is unique, as the maximum operational pressure that it can withstand, P = 100 bar, exceeds by a factor of three the technical specifications of the cells used in previous pressure-dependent X-ray reflectivity investigations (Paulus *et al.*, 2005, 2008; Lehmkühler *et al.*, 2009). In particular, its simple design, together with the availability of high-energy X-rays at the ID15A beamline of the European Synchrotron Radiation Facility (ESRF, Grenoble, France), allows us to combine the use of a large-volume see-through vessel with a high-flux and penetrating X-ray beam. In the following an example of an investigation performed at a gas/liquid interface will be described but the chamber can readily be used also for the study of gas/solid, liquid/solid and liquid/liquid interfaces.

2. Experimental

2.1. The beamline set-up

X-ray reflectivity experiments probe the vertical structure of an interface, while averaging the in-plane structure over the region that is illuminated by the X-ray beam footprint. A detailed theoretical description of X-ray reflectivity is given by Tolan (1999) and Als-Nielsen & McMorrow (2001). Here we only note that the X-ray beam impinges on the interface with a small incident angle, α_i, and is subsequently reflected. For high-energy X-rays typical values of this angle are as small as 0.01°. The reflectivity is measured as a function of the vertical momentum transfer, $q_z = (4\pi/\lambda)\sin\alpha$, by varying symmetrically the incident angle, α_i, and the exit angle, α_f, of the beam, with $\alpha_i = \alpha_f = \alpha$. Given that the index of refraction of all materials at X-ray wavelengths is slightly less than unity, total reflection at the interface occurs for all incident angles that are smaller than the critical angle, α_c, which depends on the electron density of the material and the wavelength of the X-rays.

High-energy X-ray reflectivity satisfies two apparently contradictory requirements: a high X-ray penetration power and a high surface sensitivity. Since the X-ray attenuation coefficient, μ, is a rapidly decreasing function of energy, E, with $\mu(E) \simeq E^{-3}$, high-energy X-rays can penetrate several millimeters of bulk material without much absorption. On the other hand, the use of small incident angles guarantees the surface sensitivity. A sketch of the experimental set-up in use at the ESRF's high-energy beamline ID15A is shown in Fig. 1.

A monochromatic beam, with a typical incident energy of $E \simeq 70$ keV corresponding to a wavelength, λ, of approximately 0.18 Å, is focused by a set of Al compound refractive lenses (CRL). The size of the focal spot depends on the size and the stability of the electron beam in the storage ring. The heart of the set-up is the high-energy micro-diffractometer (HEMD) (Reichert *et al.*, 2003), designed for high-energy surface and interface scattering experiments. The base of the diffractometer consists of a granite block with four granite towers. The translation and rotation motor stages are mounted on a large cradle that rests on top of the granite towers in four precision bearings. The cradle is used to define the angle, α_i, between the surface of the sample and the incoming beam: a high-resolution linear translation pulls or pushes the cradle and the precise value of the diffractometer's inclination is measured by an encoder. This high-precision mechanism is able to control α_i within 10^{-4} deg. Most importantly, an additional set of monochromator crystals (Lmono), positioned after the CRL and before the HEMD, allows the investigation of liquid surfaces by tilting the primary beam with respect to the sample (Honkimäki *et al.*, 2006). In particular, by using a pair of deflecting crystals the incident beam remains centered at a stationary sample position while the incident angle is varied. In contrast to previous liquid surface diffractometers (Als-Nielsen *et al.*, 1982; Als-Nielsen & Pershan, 1983; Pershan *et al.*, 1987; Als-Nielsen, 1999) this high-precision optical device allows the investigation of liquid surfaces without moving the sample during the measurement, hence the instabilities caused by such a mechanical disturbance are eliminated. The HEMD set-up is designed to operate with two types of detectors: point counters and two-dimensional detectors. The detector stage is designed as an independent assembly: mounted on a table, whose front and back legs can be moved with a high level of accuracy, a translation and a rotation stage ensure a precise vertical and horizontal movement of the point detector arm around the center of rotation of the diffractometer. Furthermore, the detector stage automatically follows the change of the scattering geometry when the instrument is operated in the liquid surface mode. Finally, high-energy experiments ($E \simeq 100$ keV) are especially suited for the use of two-dimensional detectors. At these energies the Ewald sphere is almost flat, making it possible to map planar projections of reciprocal space with a single exposure. For this purpose a two-dimensional detector can be mounted on the linear translation stage next to the point detector arm.

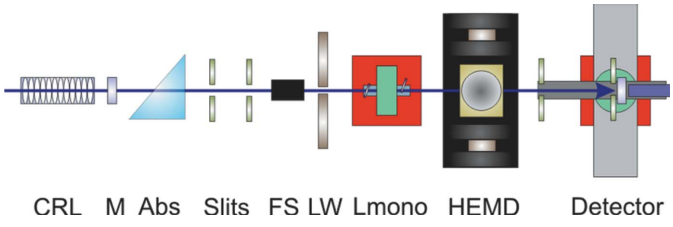

Figure 1
Schematic top view of the high-energy X-ray reflectivity set-up installed at the ID15A beamline. The first optical element is a set of Al compound refractive lenses (CRL) used to minimize the footprint of the beam impinging on the sample's surface. At low angles the intensity of the beam reflected from the sample is too high for the detector. For this reason a continuous wedge absorber (Abs) is used to attenuate the beam. Two tungsten slits and a lead wall with a pin hole (LW) remove the background radiation. A fast shutter (FS) can be brought into the beam in order to minimize the radiation dose on the sample. The monochromator for the investigation of liquid surfaces (Lmono) is positioned before the high-energy micro-diffractometer (HEMD). Two additional sets of slits are placed before the detector. Several monitors (M) are positioned along the beam path.

2.2. The pressure cell

2.2.1. The design. One of the main problems when conducting X-ray reflectivity measurements on liquid interfaces is that the presence of a macroscopically curved surface alters the profile of the reflected beam. Owing to such curvature, X-rays reflected from different regions of the surface reflect at different angles. If, in addition to the curved surface, there is also a rising meniscus at the cell windows, both the incident and the reflected beam will interfere with it. One obvious way of reducing the curvature is to maximize the dimensions of the cell. In an attempt to combine a simple design with a versatile use, a sapphire, Al_2O_3, tube has been chosen as nucleus of the custom-made pressure device schematically shown in Fig. 2. The cell is designed in such a way that the limiting factor is given by the maximum pressure, P_{max}, that can be applied to the internal wall of the cylinder without causing a failure. Indeed, in the direction parallel to the axis of the cylinder, two large stainless steel plates are

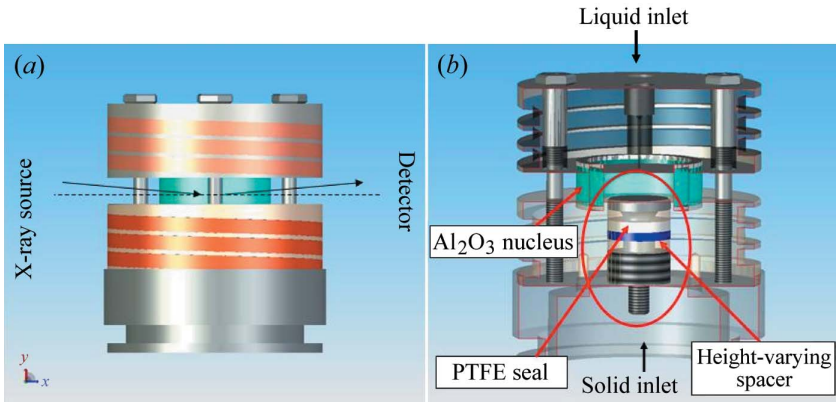

Figure 2
Schematics of the pressure cell. (*a*) Side view. The nucleus, a single crystalline Al_2O_3 ring shown in light blue, is secured by two stainless steel flanges. The black arrows indicate the direction of the incident and reflected beams. For a better visualization the relevant angles are exaggerated. The Cu pipes, used for varying the temperature, are spiraled around both stainless steel flanges and are shown in orange. (*b*) Section view. Liquid samples are introduced into the nucleus *via* a 1 mm inlet. A pressure-tight and variable-height mechanism, that allows the introduction of solid samples *via* a circular aperture machined into the bottom flange, is circled in red (see text).

bolted together *via* a variable torque mechanism, thereby sealing the internal pressure vessel on either side with two PTFE joints and ensuring the absence of leaks by appropriately adjusting the torque applied to the four bolts. A 1 mm-wide inlet, that runs through the upper flange of the cell and into the cylindrical nucleus, allows liquid samples to be inserted into the pressure vessel.

As can be seen from the cross-sectional view of the cell depicted in Fig. 2, the bottom stainless steel flange has been implemented with a 30 mm-wide pressure-tight circular aperture. Such a mechanism is crucial for the investigation of gas/solid and liquid/solid interfaces, as it allows the solid samples to be inserted into the central reservoir without having to dismantle the sapphire from the stainless steel plates. A thick PTFE joint ensures the sealing and additional spacers, shown in blue, allow the adjustment of the height of the solid surface with respect to the X-ray beam. To vary the temperature of the cell, copper tubes are spiraled around each of the two stainless steel blocks and connected to a circulating bath. A photograph of the entire pressure device is shown in Fig. 3. A multi-connector is fitted onto the top flange of the cell. Fastened to the connector are three needle valves: two of them allow the cell to be flushed with the desired gas prior to the cell being loaded and used, the third provides a connection for a roughing pump if needed. A pressure gauge and a safety valve complete the upper part of the system. Finally, the entire device is mounted onto a PTFE support. Four Al spacers and two adapter plates complete the set-up by accurately positioning the interface with respect to the incoming X-ray beam. An additional lucite shielding can be installed around the entire apparatus ensuring protection against a sudden and undesirable failure.

2.2.2. The nucleus. To a first approximation, when dealing with an ideal cylindrical vessel with $r \gg b$, where r is the inner radius and b is the wall thickness, the maximum pressure the wall can withstand in the direction perpendicular to the axis of the cylinder without failing is given by $P_{max} = \sigma b/r$, where σ is the ultimate tensile strength of the chosen material. It follows that, for a given value of P_{max}, increasing the internal diameter of the cell, as is needed if close-to-flat liquid surfaces are to be investigated, requires an increase in the wall thickness. Owing to the strong attenuation coefficients for conventional X-rays in the range 10–20 keV, large-volume gas pressure cells have, until now, been impenetrable to X-rays. In fact, both the thick walls of the cells and the long pathlengths covered by the X-ray beam traveling through the investigated bulk phases greatly attenuate the X-ray intensity that reaches the detector. The strong penetration power of high-energy X-rays provides a solution to these problems. In particular, the attenuation coefficient, μ, of X-rays penetrating sapphire at an energy of $E \simeq 70$ keV is approximately an order of magnitude smaller than the equivalent quantity for $E \simeq 20$ keV X-rays. As a consequence, macroscopic systems can be penetrated without too strong an absorption, if the dimensions and the materials are chosen with care.

Sapphire, Al_2O_3, has been chosen for its high ultimate tensile strength, its chemical inertness and its single-crystalline nature that allows reduction of the background contribution of the cell to the total scattered intensity. Given the design of the cell, a close to 360° window onto the investigated interface is offered to the incoming X-rays. An additional important

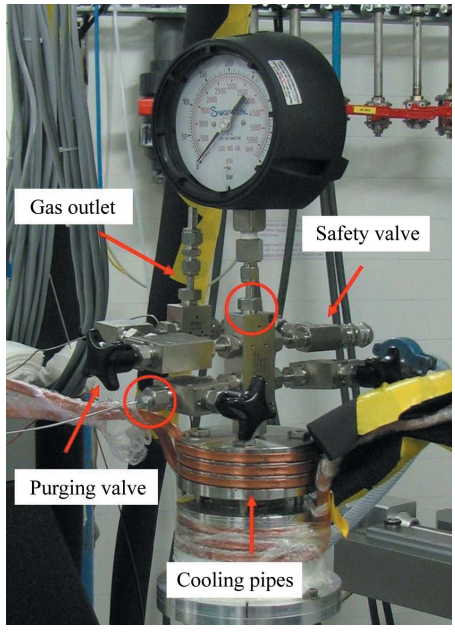

Figure 3
Photograph of the pressure device installed on the HEMD at the ID15A beamline. The gas and liquid inlets are circled in red. They are positioned at the bottom left and at the top of the multi-connector, respectively.

asset of the cell is that such a window is not only transparent to X-rays but also to the scientist's eye. The (0001)-oriented Al_2O_3 single crystal was supplied by Rubis-Precis (http://www.rubis-precis.com/). To minimize the possibility of failures, particular attention has been devoted to both the parallelism and the surface finish of the surfaces in contact with the stainless steel flanges. Added to this, Al_2O_3 is a brittle material and the presence of surface irregularities on the inner wall of the cylinder increases the probability of the vessel failing when pressurized. Therefore, the internal surface also requires a good standard polishing making the realisation of such a component extremely challenging from a technical point of view. In the particular case of the sapphire supplied by Rubis-Precis, the guaranteed average surface roughness, Ra, and parallelism of the sealing surfaces are 0.05 µm and 0.03 mm, respectively. The guaranteed Ra of the internal wall is better than 1.5 µm.

Clearly, safety is a main concern when operating large-volume gas pressure cells. In particular, it is essential for the manufacturers to be ISO9001 certified and all components must be delivered with the relevant specification sheets. Added to this, careful calculations and testing procedures are required in order to determine an accurate value for P_{max}. An Al_2O_3 cylinder has been the object of a finite-element analysis (FEA) performed with *ANSYS*. Given the symmetry of the cylinder, the calculations have been performed on one-eighth of the model, in order to improve precision. The stress components within the cylinder, caused by a pressure load that is uniformly applied to the inner wall, have been compared with the stress limit of the procured material, as certified by the manufacturer. The relevant stress limit for brittle materials under internal pressure is the ultimate tensile strength. In order to compare such quantities, a scalar is introduced: the equivalent (von Mises) stress, analytically obtained from the stress tensor components. The safety factor of a finite-element calculation describes how much the real system differs from the ideal model. To a good approximation this quantity, determined by the defects and the surface finish of the real system, is given by the ratio of the ultimate tensile stress of the material and the von Mises stress. The latter, obtained from a structural load of P_{max} = 300 bar applied to the internal wall of a sapphire cylinder whose internal diameter, external diameter and ultimate tensile strength are d_{int} = 50 mm, d_{ext} = 60 mm and σ = 392 MPa, respectively, is shown in Fig. 4. Given the good Ra value of the internal wall of our sapphire cylinder, a safety factor of approximately 2.2 is acceptable.

Finally, with a further view towards safety, the value of P_{max} has been experimentally verified by testing the entire pressure device under hydrostatic conditions. With a torque of approximately 30 Nm applied to the bolts, the sapphire cylinder fractured at P_{max} = 316 bar. Such a remarkable agreement with the FEA calculations clearly indicates that the ultimate viability of the cell presented here is determined exclusively by the sapphire. Finally, it is essential to stress that, in agreement with the safety rules of the ESRF, $P_{max}/3$ determines the maximum rated pressure of the cell, namely P = 100 bar.

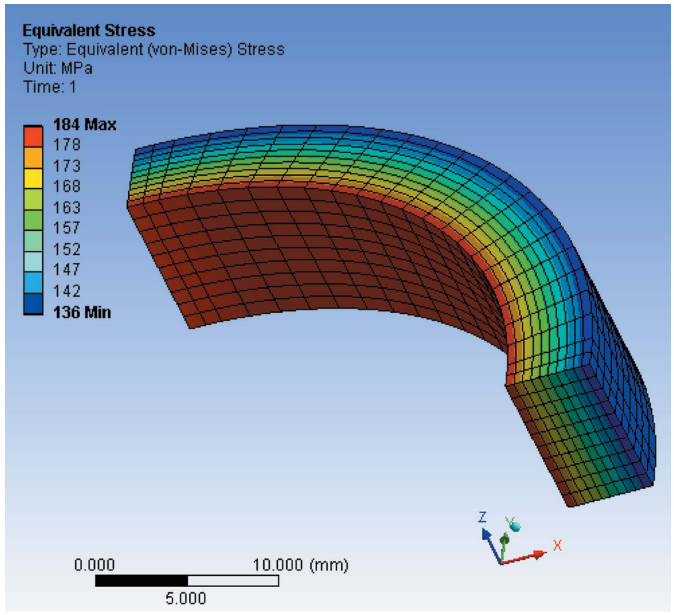

Figure 4
Equivalent (von Mises) stress obtained from finite-element calculations. The load applied uniformly on the internal wall of the Al_2O_3 nucleus described in the text is P_{max} = 300 bar. The maximum stress occurs on the inner surface of the cylinder and decreases radially.

2.2.3. The temperature control. Interfaces are highly dynamic regions that readily rearrange themselves or react in order to become energetically stable. In order to appreciate to what extent temperature is a key variable for interfacial phenomena, let us simply recall the well known temperature dependence of the surface tension (Selby, 1890). In as much as this quantity governs the shape that a small amount of liquid assumes, it can readily be understood that variable-temperature experimental devices are fundamental prerequisites to many interfacial investigations. Moreover, given the fact that a stable interface is a common requirement to all reflectivity investigations, the interfacial temperature has to be accurately controlled. In this respect, both time and care must be invested to obtain maximum temperature stability throughout each measurement.

In its current status the cell is operated in combination with an external cooling/heating system that comfortably allows control of the interfacial temperature with an accuracy of $\pm$ 0.01 K for temperatures in the 253 K $\leq T \leq$ 323 K range. In order to obtain a high thermal contact between the cell and the Cu pipes, both the latter and the spiraling grooves machined onto the blocks are square-edged. The pipes can be connected to each other, in which case a single circulating unit is needed, or they can be used independently if a temperature gradient is required between the upper and lower part of the cell. In the latter case, two independent circulating devices are used. The temperature is measured *via* two Pt100 sensors positioned, on each of the stainless steel blocks, as close as possible to the pressurized nucleus that houses the interface under investigation. In order to accurately determine the temperature of the interface itself, a careful temperature calibration has to be performed prior to each experiment.

In the case of studies that require more extreme temperatures, alternative heating/cooling options can be envisaged. Despite it being a rather time-consuming procedure for more extreme temperatures, varying the temperature of the entire system with the aid of external cooling/heating devices is possible, as the working temperature range of most circulating baths is wide. However, in this case the use of an external insulating protection is highly recommended. Conventional temperature-regulating devices that require electrical feedthroughs could also be installed within the pressurized nucleus, although particular attention is necessary in order not to compromise the capacity of the cell to withstand relatively high pressures. Lastly, given the transparency of Al_2O_3 to most wavelengths, the use of radiative heating devices that are able to locally increase the temperature of the interface in a non-invasive manner is an additional possibility.

3. Gas hydrate research: an example of an application

Gas hydrates (Sloan & Koh, 2008) are non-stoichiometric inclusion compounds that exist in a stable and solid phase when small gas molecules come in contact with water at moderate pressures and low temperatures. What was, initially, a purely academic curiosity in gas hydrates has recently become a widespread interest triggered by the function that these compounds play in both natural and industrial environments. In the particular case of methane hydrates, a complete understanding of their formation and decomposition processes would allow for a safe extraction of natural gas from the vast reservoirs discovered in marine and permafrost sediments, the transport and storage of such gas in hydrate form, and for a better understanding of the role that methane hydrates play in our planet's climate stability.

Although much is known about the structure of gas hydrates, the question of how they form at a molecular level is still very much unanswered. Bulk neutron diffraction and high-energy X-ray diffraction experiments at high gas pressures (Chazallon & Kuhs, 2002; Staykova *et al.*, 2003; Klapproth *et al.*, 2003; Kuhs *et al.*, 2006) have proven their usefulness in obtaining both detailed structural information and a better understanding of the kinetics of hydrate formation and growth from bulk powdered ice. Interfacial investigations have shown that hydrate formation is, indeed, an interfacial phenomenon (Sugaya & Mori, 1996; Uchida *et al.*, 1999; Ohmura *et al.*, 2000; Kobayashi *et al.*, 2001; Freer *et al.*, 2001; Taylor *et al.*, 2007). It is nowadays known that, after a period of two-phase contact, that precedes nucleation and is referred to as the induction time, a hydrate film forms and rapidly covers the gas/water interface. Nevertheless, a truly microscopic understanding of the interfacial mixing between liquid water and the relevant gas under hydrate-forming conditions is largely missing today, as the resolution of the majority of previous interfacial investigations has been limited to the micrometer range. Indeed, very few experimental methods are able to provide data with atomic resolution from liquid interfaces under pressure. X-ray reflectivity has, however, been used to determine the adsorption isotherms at the propane/water interface for pressures close to the condensation pressure of propane (Paulus *et al.*, 2008). For higher pressures, that require the use of thick-walled cells, such studies are impossible with X-rays belonging to a conventional energy range. Furthermore, although neutrons have the penetration depth necessary to overcome this technical problem, the background-limited dynamic range probed by neutron reflectivity experiments puts severe restrictions on the obtainable resolution. Hence, an *in situ* high-resolution investigation of gas hydrate formation at the guest/host interface, *i.e.* gas/liquid and liquid/liquid, has only recently been published (Lehmkühler *et al.*, 2009).

The cell described in this manuscript is ideal for similar investigations. Most importantly, the device can withstand experimental pressures up to 100 bar, *i.e.* close to three times the maximum working pressure reached before (Lehmkühler *et al.*, 2009). This allows us to explore rather large portions of the gas hydrate stability regions. In the very relevant case of methane hydrates formed from liquid water, the entire stability region relative to 273 K $\leq T \leq$ 286 K can be explored with the use of our cell. Hence, given the important role these compounds play in modern-day energy and environmental issues, the investigation of the methane/water interface as a function of pressure will be briefly discussed as an appropriate first experimental challenge for this newly built device.

Temperature and pressure, T and P, respectively, together with the solubility of the chosen gas in water, are the key parameters that govern gas hydrate phenomena. In the particular case of CH_4, its solubility in H_2O is very low and, as a result, the induction time that precedes the nucleation of CH_4 hydrate crystals is particularly long. In order to perform a controlled and well defined experiment the temperature of the system has been kept constant, T = 282.7 K, and the reflectivity curves have been measured for two different values of P, namely P = 1 bar and P = 100 bar. The results are shown in Fig. 5. The measured dynamic range exceeds 10^{-8}, allowing us to reach, for the low-pressure measurement, a maximum value for the vertical momentum transfer, $q_{z\,\max} = (4\pi/\lambda)\sin\alpha_{\max}$, of

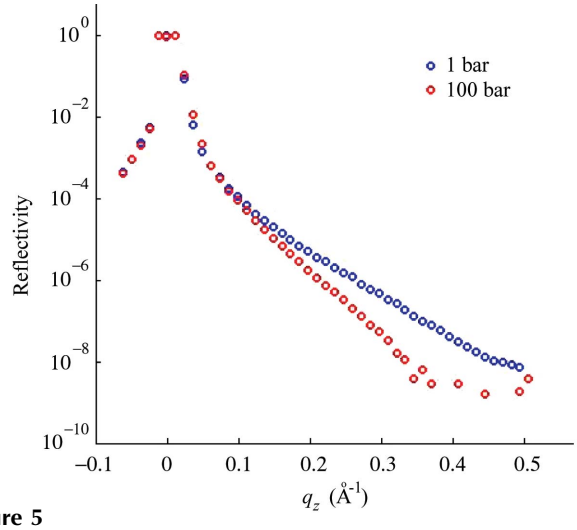

Figure 5
Reflectivity curves of the CH_4/H_2O interface measured as a function of pressure. Blue: P = 1 bar. Red: P = 100 bar.

approximately 0.45 Å for an incoming wavelength, λ, of 0.18 Å. For P = 100 bar, the equilibrium methane hydrate formation temperature is $T_{\rm equilibrium} \simeq 286$ K. The choice of a lower experimental temperature, T = 282.7 K, places the system well within the methane hydrate stability region. On the contrary, the (P, T) = (1 bar, 282.7 K) thermodynamic point is chosen to be outside such a region.

From our observations we can, with confidence, exclude the onset of hydrate nucleation. Indeed, nucleation is known to be followed by the rapid growth of a well defined interfacial film that has not been detected. At high pressure, however, we observe a steeper decay of the measured reflectivity if compared with the low-pressure data. This can only be due to an increase in roughness or to the presence of an interfacial structure whose electron density differs from the values of the two bulk phases. We have no indication of a change in interface roughness with pressure. Therefore we conclude that the observed effect is related to the interfacial mixing of water and methane prior to hydrate nucleation. A detailed analysis of this phenomenon is beyond the scope of this manuscript and will be presented elsewhere.

4. Conclusions

A new experimental set-up that is capable of measuring high-quality high-energy X-ray reflectivity data from interfaces under pressure has been described. To demonstrate the potential of the new pressure cell, we have chosen to investigate the gas/liquid interface between CH_4 and H_2O, of particular importance in gas hydrate research. During the time scale of our observation, methane hydrate nucleation has not taken place. We believe that it is precisely the absence of nucleation that allows us to experimentally access the unexplored world of gas hydrate pre-nucleation phenomena. Further analysis and experiments are expected to provide unprecedented molecular-scale information regarding the very early stages of gas hydrate formation.

We thank S. De Panfilis and D. Pontoni for welcome discussions and help in commissioning the cell.

References

Als-Nielsen, J. (1999). *Synchrotron Radiat. News*, **12**, 5–9.
Als-Nielsen, J., Christensen, F. & Pershan, P. S. (1982). *Phys. Rev. Lett.* **48**, 1107–1110.
Als-Nielsen, J. & McMorrow, D. (2001). *Elements of Modern X-ray Physics.* New York: Wiley.
Als-Nielsen, J. & Pershan, P. S. (1983). *Nucl. Instrum. Methods*, **208**, 545–548.
Baigl, D., Sferrazza, M., Guedeau-Boudeville, M.-A., Ober, R., Rieutord, F., Theodoly, O. & Williams, C. E. (2005). *J. Phys. Condens. Matter*, **17**, 6329–6336.
Bertrand, E., Dobbs, H., Broseta, D., Indekeu, J., Bonn, D. & Meunier, J. (2000). *Phys. Rev. Lett.* **85**, 1283–1285.
Chazallon, B. & Kuhs, W. F. (2002). *J. Chem. Phys.* **117**, 308–320.
Dysthe, D. K., Wogelius, R. A., Tang, C. C. & Nield, A. A. (2006). *Chem. Geol.* **230**, 232–241.
Engemann, S., Reichert, H., Dosch, H., Bilgram, J., Honkimäki, V. & Snigirev, A. (2004). *Phys. Rev. Lett.* **92**, 205701.
Freer, E. M., Selim, M. S. & Sloan, E. D. (2001). *F. Ph. Equil.* **185**, 65–75.
Galle, C. (2000). *Appl. Clay Sci.* **17**, 85–97.
Grunwaldt, J.-D. & Baiker, A. (2005). *Phys. Chem. Chem. Phys.* **7**, 3526–3539.
Grunwaldt, J.-D., Ramin, M., Rohr, M., Michailovski, A., Patzke, G. R. & Baiker, A. (2005). *Rev. Sci. Instrum.* **76**, 541041.
Honkimäki, V., Reichert, H., Okasinski, J. S. & Dosch, H. (2006). *J. Synchrotron Rad.* **13**, 426–431.
Huisman, W. J., Peters, J. F., Zwanenburg, M. J., de Vries, S. A., Derry, T. E., Abernathy, D. & van der Veen, J. F. (1997). *Nature (London)*, **390**, 379–381.
Klapproth, A., Goreshnik, E., Staykova, D., Klein, H. & Kuhs, W. F. (2003). *Can. J. Phys.* **81**, 503–518.
Kobayashi, I., Ito, Y. & Mori, Y. H. (2001). *Chem. Eng. Sci.* **56**, 4331–4338.
Kuhs, W. F., Staykova, D. K. & Salamatin, A. N. (2006). *J. Phys. Chem. B*, **110**, 13283–13295.
Lehmkühler, F., Paulus, M., Sternemann, C., Lietz, D., Venturini, F., Gutt, C. & Tolan, M. (2009). *J. Am. Chem. Soc.* **131**, 585–589.
MacDonald, A. G. (1984). *Philos. Trans. Soc. London Ser. B*, **304**, 47–68.
Mezger, M., Schöder, S., Reichert, H., Schröder, H., Okasinski, J. S., Honkimäki, V., Ralston, J., Bilgram, J. & Dosch, H. (2008a). *J. Chem. Phys.* **128**, 2447051.
Mezger, M., Schröder, H., Reichert, H., Schramm, S., Okasinski, J. S., Schöder, S., Honkimäki, V., Deutsch, M., Ocko, B. M., Ralston, J., Rohwerder, M., Stratmann, M. & Dosch, H. (2008b). *Science*, **322**, 424–428.
Miller, C. E., Majewski, J., Gog, T. & Kuhl, T. L. (2005). *Phys. Rev. Lett.* **94**, 238104.
Ohmura, R. Kashiwazaki, S. & Mori, Y. H. (2000). *J. Cryst. Growth*, **218**, 372–380.
Paulus, M., Gutt, C. & Tolan, M. (2005). *Phys. Rev. E*, **72**, 061601.
Paulus, M., Gutt, C. & Tolan, M. (2008). *Surf. Interface Anal.* **40**, 1226–1230.
Pershan, P. S., Braslau, A., Weiss, A. H. & Als-Nielsen, J. (1987). *Phys. Rev. A*, **35**, 4800–4813.
Ragil, K., Meunier, J., Broseta, D., Indekeu, J. O. & Bonn, D. (1996). *Phys. Rev. Lett.* **77**, 1532–1535.
Reichert, H., Honkimäki, V., Snigirev, A., Engemann, S. & Dosch, H. (2003). *Physica B*, **336**, 46–55.
Reichert, H., Klein, O., Dosch, H., Denk, M., Honkimäki, V., Lippmann, T. & Reiter, G. (2000). *Nature (London)*, **408**, 839–841.
Richter, A. G., Yu, C.-J., Datta, A., Kmetko, J. & Dutta, P. (2000). *Phys. Rev. E*, **61**, 607–615.
Rieutord, F., Eymery, J., Fournel, F., Buttard, D., Oeser, R., Plantevin, O., Moriceau, H. & Aspar, B. (2001). *Phys. Rev. B*, **63**, 125408.
Roser, S. J., Felici, R. & Eaglesham, A. (1994). *Langmuir*, **10**, 3853–3856.
Schlossman, M. L. (2005). *Physica B*, **357**, 98–105.
Schöder, S., Reichert, H., Schröder, H., Mezger, M., Okasinski, J. S., Honkimäki, V., Bilgram, J. & Dosch, H. (2009). *Phys. Rev. Lett.* **103**, 095502.
Selby, A. L. (1890). *Proc. Phys. Soc. London*, **11**, 119–122.
Sloan, E. D. & Koh, C. A. (2008). *Clathrate Hydrates of Natural Gases*, 3rd ed. Boca Raton: CRC Press.
Staykova, D. K., Kuhs, W. F., Salamatin, A. N. & Hansen, T. (2003). *J. Phys. Chem. B*, **107**, 10299–10311.
Sugaya, M. & Mori, Y. H. (1996). *Chem. Eng. Sci.* **51**, 3505–3517.
Taylor, C. J., Miller, K. T., Koh, C. A. & Sloan, E. D. (2007). *Chem. Eng. Sci.* **62**, 6524–6533.
Tikhonov, A. M., Pingali, S. V. & Schlossman, M. L. (2004). *J. Chem. Phys.* **120**, 11822–11838.
Tolan, M. (1999). *X-ray Scattering from Soft-Matter Thin Films*, *Springer Tracts in Modern Physics*, Vol. 148. Berlin: Springer.
Uchida, T., Ebinuma, T., Kawabata, J. & Narita, H. (1999). *J. Cryst. Growth*, **204**, 348–356.